buildings

MDPI

Article

Seismic Response of the Continuous Rigid-Framed Bridge with Super-High Piers Based on Shaking Table Tests

Xiao-Yu Yan [1], Zhuo Zhao [2], Shan-Shan Cao [1,*], Ya-Fen Zhang [1] and Cong-Hui Liu [2]

[1] School of Engineering, The Open University of China, Beijing 100039, China
[2] Key Laboratory of Urban Security and Disaster Engineering of China Ministry of Education, Beijing University of Technology, Beijing 100124, China
* Correspondence: caoss@ouchn.edu.cn

Abstract: Continuous rigid-framed bridges with super-high piers (CRFB-HP) have been widely applied in mountain areas. However, their seismic performance is still urgently to be clarified. In this study, the refined finite element model (FEM) of a CRFB-HP was constructed and verified according to the shaking table test results of its scaled model. On this basis, systematic elastic-plastic time history analysis of the CRFB-HP was conducted to investigate the influence of parameters on their seismic performance, including main bridge span, pier height and number of tie beams. The results show that CRFB-HP have the characteristic of long vibration periods and are more sensitive to long-period ground motions. Along the longitudinal and transverse directions, the peak pier top displacement and pier bottom bending moment of CRFB-HP are both relatively large under NLPL (+20~+70%) and NFPT ($T_P \approx T_1$, +50~+120%) excitations. For the same span, the peak pier top displacement increases with the pier height increasing, while the peak pier bottom bending moment decreases with the pier height increasingFor the same pier height, the peak pier top displacement and peak pier bottom bending moment both increase with the span length increasing. Moreover, the pier height change has a greater effect on the pier top displacement than that of the span change. CRFB-HP show obvious high-order response participation (HRP) under different ground motions. The NFPT ($T_P \approx T_1$), ground motions can significantly increase HRP. Moreover, compared with cast-in-place CRFB-HP, the HRP of a fabricated super-high pier is greater (+20~+30%). The peak pier top displacement and pier bottom bending moment both decrease with the increase in the number of tie beams. The reasonable arrangement of tie beams can improve the lateral seismic performance of CRFB-HP. However, compared to the cast-in-place CRFB-HP, the peak pier top displacement is larger, and the peak pier bottom bending moment is smaller, for the fabricated CRFB-HP.

Keywords: super-high pier; continuous rigid-framed bridge; seismic response; shaking table test

Citation: Yan, X.-Y.; Zhao, Z.; Cao, S.-S.; Zhang, Y.-F.; Liu, C.-H. Seismic Response of the Continuous Rigid-Framed Bridge with Super-High Piers Based on Shaking Table Tests. *Buildings* **2024**, *14*, 1527. https://doi.org/10.3390/buildings14061527

Academic Editor: Fabrizio Gara

Received: 11 April 2024
Revised: 20 May 2024
Accepted: 22 May 2024
Published: 24 May 2024

1. Introduction

With the construction of railways and expressways in western mountainous areas of China, bridge structures have been developing in the direction of high piers and long spans [1–3]. Chinese relevant codes have not yet given a clear definition of super-high piers. Drawing on the concept of super-high-rise buildings in civil building standards [4], a pier height of more than 100 m and a calculation of the first-order vibration mass participation coefficient of less than 60% is defined as a super-high pier [5]. At this stage, scholars have made a certain degree of progress in the study of super-high-pier structures. When analyzing the seismic performance of extremely tall piers, Xu et al. [6] introduced a simplified single-degree-of-freedom (SDOF) system that disregarded high-order modes, along with a more complex multi-degree-of-freedom (MDOF) system that took into account these high-order modes. Their study focused on evaluating the seismic behavior of group pile foundations in B-SHPs. The results indicate that neglecting the contribution of higher-order modes may significantly underestimate the seismic demand of pile foundations. Another

study by Xu [7] has demonstrated that, unlike medium and low piers, the curvature at the bottom of the pier in SHPs shows less correlation with the displacement at the top of the pier, attributed to the influence of high-order modes. Tubaldi et al. [8] analyzed the vibration modes of B-SHPs through theoretical and numerical methods. Their findings indicated that the mass participation ratio of the first-order mode in SHPs remained relatively consistent despite changes in axial load. In contrast, the mass participation ratio of higher-order modes was significantly affected by axial load variations, highlighting the importance of considering the impact of these modes on the seismic response of SHPs. Li et al. [9] highlighted that the weight of the substructure was frequently greater than that of the superstructure, leading to significant internal force requirements. Shao et al. [10] studied the longitudinal damping performance of a continuous steel truss bridge with seismic high piers (SHPs) using numerical simulation and various parameters of viscous dampers. Their findings revealed that the damping behavior of viscous dampers in the B-SHP differed from that of bridges with low and medium piers due to the influence of high-order modes. It is crucial to consider the plastic development in the middle of the pier during seismic design of SHPs. Furthermore, Xu, Shen, and Luo et al. [11–13] conducted research on the seismic behavior of exceptionally tall buildings using shaking table experiments. Their findings highlighted the importance of taking into account high-order modes in the seismic assessment and design of such structures. In addition, the vulnerability of high-pier bridges [14,15], seismic risk evaluation [16] and soil–structure interaction [17] have also been studied by some scholars. In summary, compared with regular bridges, super-high-pier continuous rigid-frame bridges are characterized by high flexibility of piers, large structural period and significant effects of high-order modes of vibration. Especially, the effects of distributed masses and high-order modes of piers should not be ignored in the seismic analysis and design of bridges with super-high piers. However, there are no universally applicable laws, industry codes and standards in practical engineering applications. Therefore, it is necessary to conduct further research on super-high-pier bridges.

Moreover, to solve the problems of difficult construction, long construction period and environmental impact in the construction process of SHPs, fabricated technology [18,19] was regarded as the development direction of SHPs. The introduction of fabricated joints would cause the construction and seismic performance of fabricated SHPs to be more complex [20,21]. However, the existing seismic analysis and tests of bridges rarely involve SHPs or B-SHPs (especially fabricated super-high piers, SHP-Fs). Research on the seismic response law of super-high piers with cast-in-place or fabricated connections (SHP-Cor SHP-Fs) urgently needs to be conducted. More attention should be paid to the seismic performance of fabricated super-high piers. The current research in this part mainly focuses on the simulation and test research of bridge piers, including quasi-static analysis of middle and low piers and shaking table tests of single piers [22,23]. There is little research on the seismic performance of integral bridges, especially continuous rigid-framed bridges with fabricated super-high piers, and systematic theoretical research is lacking. The application of assembly-type technology to complex engineering structures such as super-high piers is still in the exploration stage, and the application effect of existing assembly-type technology in super-high piers is still to be verified.

In this study, the super-high-pier continuous rigid bridge across a V-shaped deep valley was taken as the research background. The refined finite element model (FEM) of a CRFB-HP was constructed and verified according to the shaking table test results of its scaled model. On this basis, systematic elastic-plastic time history analysis of the CRFB-HP was conducted to investigate the influence of parameters on their seismic performance, including main bridge span, pier height and number of tie beams.

2. Engineering Background

The prototype bridge was a continuous rigid-framed bridge with cast-in-place super-high piers over a V-shaped deep valley. The span was 88 m + 166 m + 88 m, as shown in Figure 1a. The heights of the main piers were 100 m. The width of the bridge deck was 25 m.

The superstructure was a prestressed concrete single-box, single-room, variable-section box beam, as shown in Figure 1b. The root section height of the main beam was 10.0 m, the middle section and the end section heights of the main beam were 3.5 m. The width of the top plate of the box beam was 12.5 m, and the width of the bottom plate was 7.5 m. The main beam was made of C55, whose compression strength was 55 MPa. The curve at the bottom of the beam was a quadratic parabola. The substructure comprised reinforced concrete hollow thin-walled piers with a linear variable section. The pier was a thin-walled pier with a boxed section, as shown in Figure 1c. The concrete type of the piers was C40, whose compression strength was 40 MPa. A tie beam was arranged at half the height of the pier, as shown in Figure 1d. The cross section of the tie beam was a square, and the size was 250 cm × 250 cm. The seismic fortification intensity of the bridge was 8 degrees.

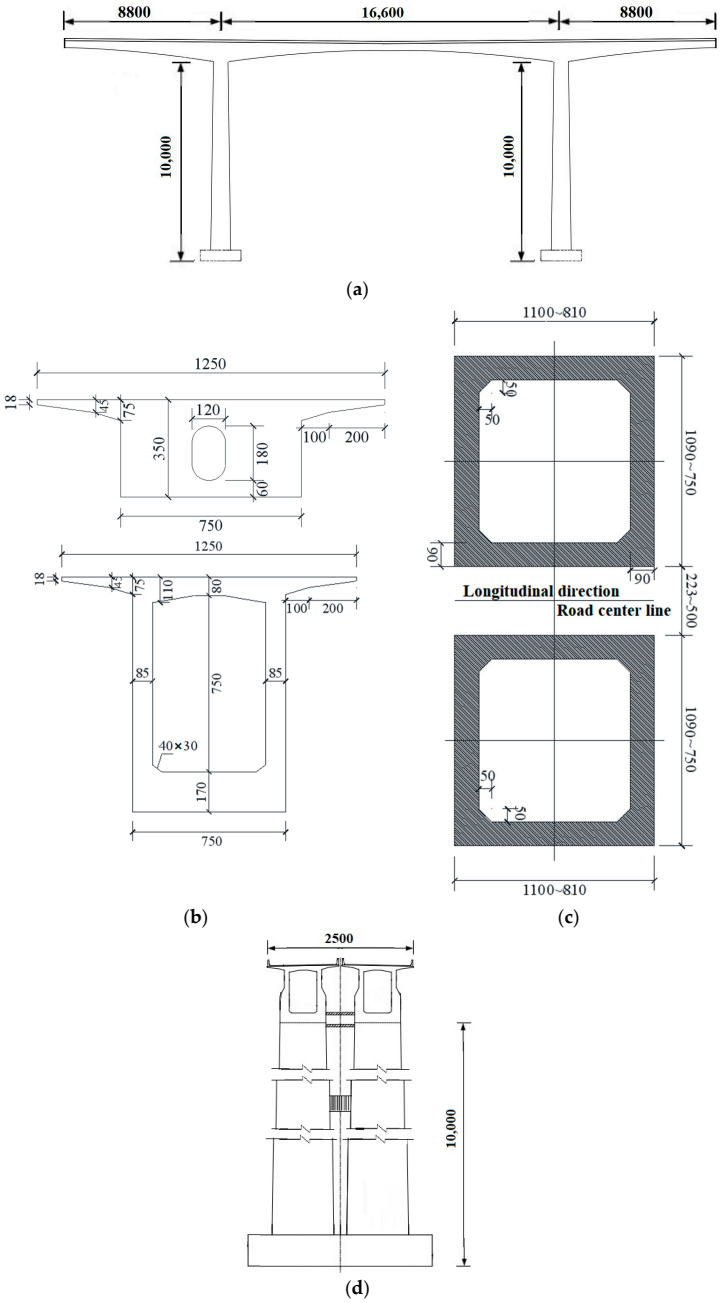

Figure 1. Structural dimensions of the prototype bridge (unit: cm): (**a**) External dimensions of the bridge specimen; (**b**) Sections of the main beam; (**c**) Sections of the pier; (**d**) Cross section of the bridge.

Grouting sleeves have the advantages of simple structure, good connection performance and economy [24,25]. Accordingly, based on the design parameters of the prototype bridges, we designed a fabricated bridge model, also based on the research results of the seismic performance of fabricated concrete piers connected with grouting sleeves [23,26]. In practical application, the grouting sleeve–prestressing combined connection method for super-high piers has been proposed by the authors, shown in Figure 2. The multi-configuration fabricated pier wall and the cast-in-place bearing platform are connected by grouting sleeves; the vertical multi-configuration fabricated pier wall segments are connected by grouting sleeves, while the horizontal ones are connected by local cast-in-place nodes and annular prestressed tendons. This kind of fabricated super-high piers can effectively improve the effectiveness of segment connection and the integrity of fabricated components, and was selected as the prototype of the fabricated model pier [26].

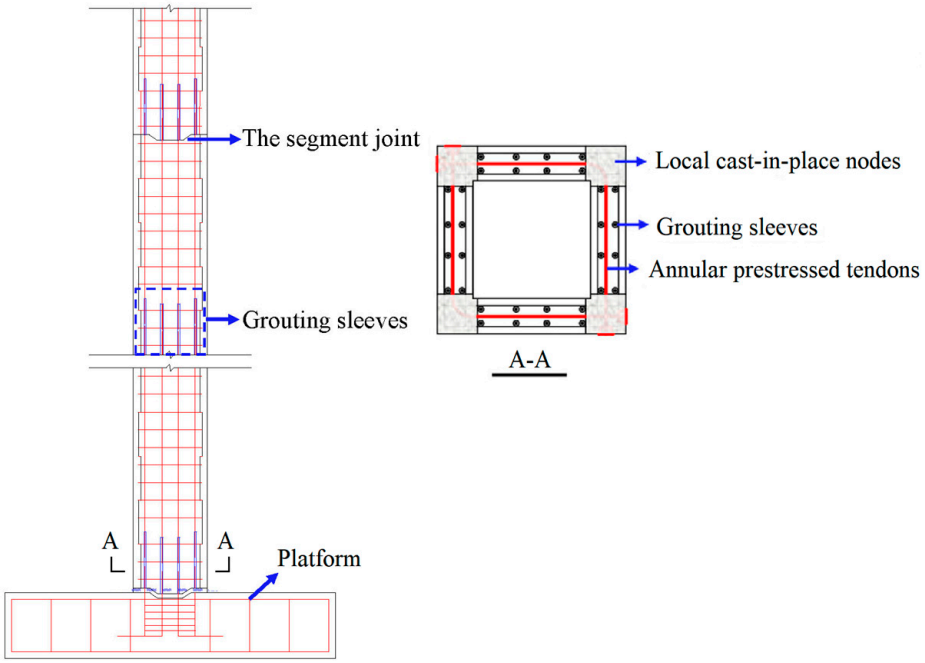

Figure 2. Grouting sleeve connection diagram.

3. Finite Element Model and Experimental Verification

3.1. Finite Element Model and Experimental Verification for a Single Pier

3.1.1. Finite Element Model for a Single Pier

The FEM of the single pier was established by Open System for Earthquake Engineering Simulation (OpenSees), which is recommended by the Network for Earthquake Engineering Simulation (NEES) and the Pacific Earthquake Engineering Research Center (PEER). In practical engineering, the pier is in an elasto-plastic state under strong earthquake excitation. Therefore, a nonlinear beam-column fiber element was used to simulate an established super-high pier. As shown in Figure 3,the plastic hinges of the element were simulated by the fiber section. A zero-length section element was used to simulate the segment joints. As shown in Figure 4 and Table 1, the Concrete02 material object was selected as the constitutive model of the concrete, and the Giuffre–Menegotto–Pinto (Steel02) material object was selected as the constitutive model of the reinforcement. The grouting sleeve connection area was set at 5 m intervals along the pier height. Elastic Uniaxial Material was used to simulate the grouting sleeves. The annular prestressing tendons was simulated by a Truss element and Steel02 constitutive relationship. The main bridge pier–girder connection was simulated by a Rigid Link Beam.

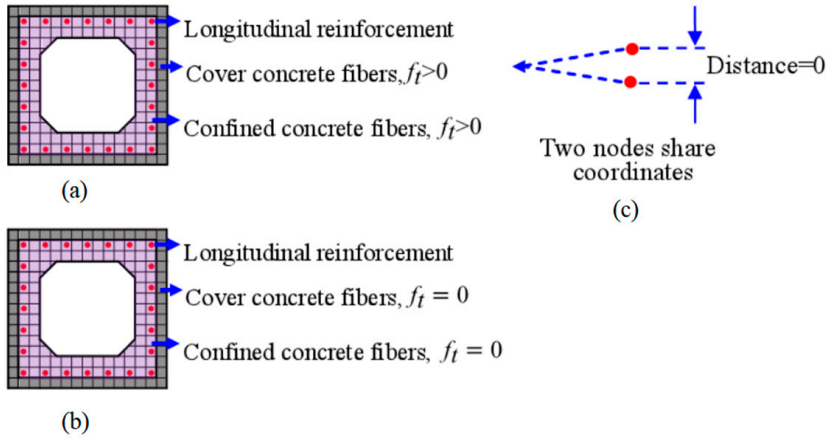

Figure 3. Details of the simulation of the piers: (**a**) Fiber section of the pier; (**b**) Fiber section of pier joint; (**c**) segment joints (zero length element).

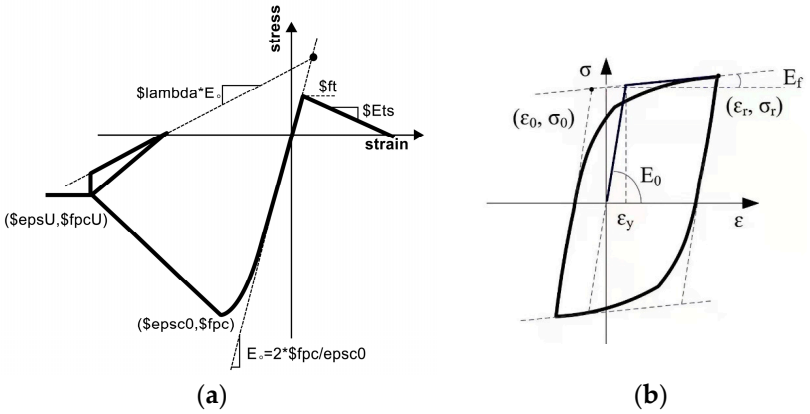

Figure 4. Constitutive of materials: (**a**) Concrete02 model; (**b**) Giuffré–Menegotto–Pinto (Steel02).

Table 1. Mechanical parameters of C40.

C40		f_{pc}/MPa	epsc0	f_{pcu}/MPa	epscu	f_t/MPa	Ets/MPa
Concrete02	cover concrete	−21.2	−0.0020	−4.2	−0.0035	2.4	1625
	confined concrete	−26.2	−0.0025	−5.2	−0.0190	2.6	1625

3.1.2. Shaking Table Test for a Single Pier

The prototype bridge was scaled down according to S_L = 1/20 according to the similarity principle, laboratory site and equipment conditions. To consider the frame effect of CRFB [7,27], the similarity of the dynamic characteristics of the prototype bridge were selected as the design principle of the bridge model, and the prototype bridge was simplified to a "T"-shaped structure. The main components of the "T" structure included the upper main beam, middle pier and lower bearing platform, with a total height of 5.5 m [26]. The key similarity coefficients of the test model are summarized in Table 2. A single-box, single-room concrete section was used. The height of the box beam changed linearly along the longitudinal bridge direction. The root height and end section height of the main beam were 300 mm and 175 mm, respectively. The width of the box beam was 600 mm. The main beam used C55. The longitudinal reinforcements of the beam were Φ6 with a ratio of 3.1%. The stirrups of the beam were Φ6 with a ratio of 1.2%. Stirrup spacing was 135 mm. A hollow thin wall pier was adopted consistent with the prototype structure. The height of the pier was 5 m. The concrete type of the pier was C40. The cross-sectional size of the pier was 300 mm × 330 mm, and the wall thickness was 65 mm. The longitudinal reinforcements of the pier were HRB400 with a yield strength of

400 MPa. The diameter was 14 and the ratio of reinforcement was 2.1%. The stirrups of the pier were HPB300 with a yield strength of 300 MPa. The diameter was 6 and the ratio of reinforcement was 1.9%. Stirrup spacing was 80 mm, and encrypted to 70 mm within 1.0 m from the pile cap. The proportion of stirrup in the bearing cap and its vicinity was 2.1%. The superstructure weight of the continuous rigid bridge with a super-high pier was simulated by adding counterweights to the pier body to regulate the similarity ratio of the mass density, as shown in Figure 5. A gasket was placed between the steel brick and the pier to prevent the hoop effect. Due to the limitation of laboratory conditions, the reinforced concrete cap of the prototype bridge was replaced by a steel cap, with a cross diaphragm and a steel cofferdam, and filled with high-strength grouting material to enhance the grip of the steel bar. The longitudinal reinforcement and stirrup extend into the upper main beam and the bottom cap, respectively, with an extension length of 200 mm. At the same time, a 135° bend hook with a length of 100 mm was set in the part extending into the main beam of the pier. The pier was connected to the shaking table through the bottom steel cap to simulate the boundary condition of the pier bottom consolidation.

Table 2. The key similarity coefficients of the test model.

Parameter	Dimension	Scale Factor
Length	[L]	$S_L = 1/20$
Elastic Modulus	$[FL^{-2}]$	$S_E = 1$
Density	$[FT^2L^{-4}]$	$S_\rho = 1$
Equivalent Mass Density	$[FT^2L^{-4}]$	$S_{\rho 0} = 4$
Time	[T]	$S_t = (S_L S_a)^{0.5} = 0.1$
Acceleration	$[LT^{-2}]$	$S_a = 5$

Figure 5. Accessory quality.

The strain sensors, acceleration sensors and displacement sensors were arranged along the height of the pier to obtain the strain, acceleration, displacement responses and section

mean curvature of the key positions of the specimen. The arrangement of the measurement points is shown in Figure 6.

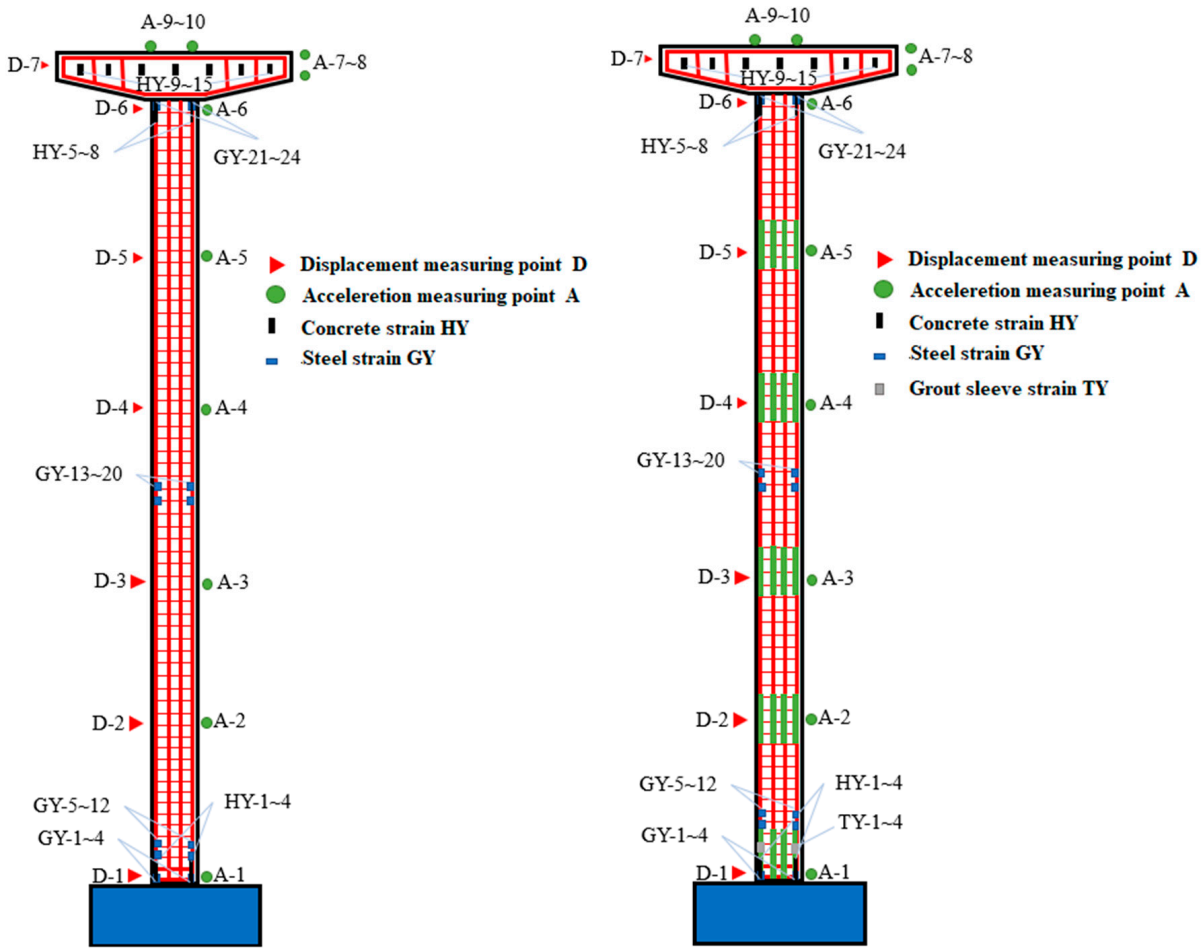

Figure 6. Layout of the measuring points.

3.1.3. Experimental Verification for a Single Pier

In this part, the FEM established in Section 3.1.1 was verified by shaking table test done in Section 3.1.2 and the FEM established by Midas.

White noise sweeping was used to obtain the dynamic characteristics of the bridge specimen. It was applied along the longitudinal bridge. By analyzing the autopower spectral density (PSD) and cross power spectral density (CPSD) of the acceleration response of a model bridge and performing normalization processing, the first three vibration modes of the structure and their corresponding frequencies can be identified. The steps are as follows:

1. Acquisition of acceleration response data is performed at various elevations along the bridge pier, specifically at heights of 2 m, 4 m, 6 m, 8 m and 10 m.
2. The autopower spectral density (PSD) and cross power spectral density (CPSD) of the acceleration responses at points with heights H = 2 m, 4 m, 6 m, 8 m and 10 m are calculated.

The autopower spectral density describes the variation of power distribution of the acceleration signal at a single accelerometer measurement point with respect to frequency. The calculation formula is as follows:

$$PSD_{ii}(f) = \frac{1}{2\pi}|A_i(f)|^2,$$

where $A_i(f)$ is the Fourier transform of the acceleration signal.

The cross power spectral density (CPSD) describes the cross-spectral density of the acceleration signals between two accelerometer measurement points. The calculation formula is as follows:

$$CPSD_{ij}(f) = \frac{1}{2\pi} A_i(f) A_j^*(f),$$

where $A_j^*(f)$ is the complex conjugate of the Fourier transform of the acceleration signal at point j.

3. To ensure comparability across different measurement points, the cross power spectral densities derived in step 2 are subjected to normalization, yielding the normalized cross power spectral densities.
4. The structural natural frequencies for each mode are identified by locating the peaks in the autopower spectral density.
5. The vibration modes can be reconstructed using the cross power spectral densities at the identified natural frequencies. At these frequencies, the amplitude of the cross power spectral density is directly proportional to the relative displacement between any two measurement points. The phase differences within the cross power spectral densities allow for the determination of the direction and phase relationships of the structural vibrations. The graphical representation of these vibration modes, as deduced from steps 1 through 5, corresponds to the modes depicted in Figure 7 of the manuscript.

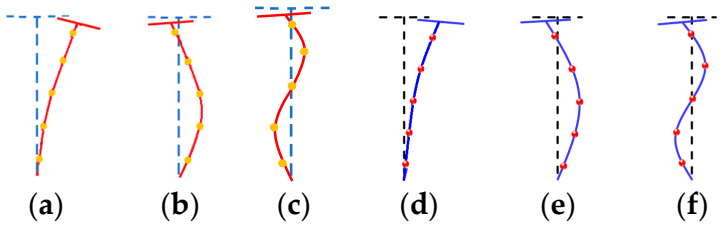

Figure 7. Vibration mode in longitudinal direction of the cast-in-place bridge specimen: (**a**) First Mode (experiment); (**b**) Second Mode (experiment); (**c**) Third Mode (experiment); (**d**) First Mode (OpenSees); (**e**) Second Mode (OpenSees); (**f**) Third Mode (OpenSees).

The vibration modes and frequencies obtained from the experiment were compared with the results derived from the FEM established by OpenSees. The vibration modes of the cast-in-place super-high pier and the fabricated super-high pier were basically consistent. So, in this paper, the accuracy of the extracted vibration modes from the numerical model was verified using the example of a cast-in-place bridge pier. From Figure 7a–c, it can be seen that the first vibration mode in the longitudinal bridge direction is longitudinal drift. The second vibration mode is bending, and the third vibration mode is high-order bending. The high-order vibration modes of the experimental model bridge pier are excited, which is consistent with the modes obtained through finite element software in Figure 7d–f. As shown in Table 3, the error between the values calculated by FEM and obtained by experiment ranges from 0.67% to 2.55%, which was basically consistent.

Table 3. Comparison between experimental and calculated results for the dynamic characteristics.

Structural Style	Vibration Mode	Experimental Value (Hz)	OpenSees (Hz)	Error (%)
Cast-in-place super-high pier	1	2.75	2.82	2.55
	2	18.23	18.35	0.67
	3	49.24	48.05	2.42
Fabricated super-high pier	1	2.88	2.95	2.43
	2	18.95	19.01	0.32
	3	51.6	52.02	0.81

Taking the RSN40 ground motion as an example, the accuracy of the FEM was verified. Figure 8 shows the displacement time–history curves of the cast-in-place super-high piers and fabricated super-high piers under RSN40 excitation. The peak of the acceleration was 1.5 g.

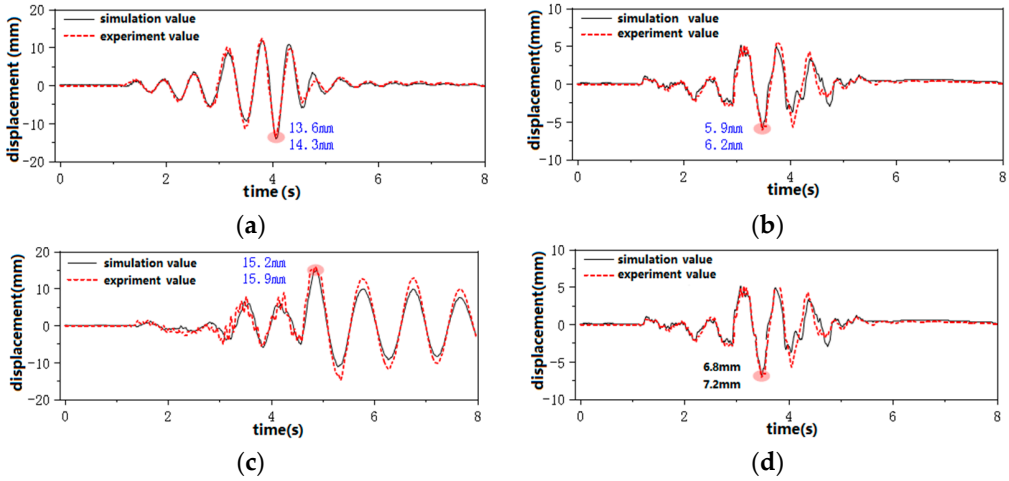

Figure 8. Displacement time course curve of the super-high piers under RSN40 excitation: (**a**) H = 5 m (cast-in-place); (**b**) H = 2 m (cast-in-place); (**c**) H = 5 m (fabricated); (**d**) H = 2 m (fabricated).

As shown in Figure 8, the peak pier top displacement of the cast-in-place super-high pier was 14.3 mm as calculated by the FEM, and 13.6 mm as measured by the test, with an error of 5.1%. The peak displacement at 2 m of the pier body was 5.9 mm as calculated by the FEM, and at 6.2 mm as measured by the test, with an error of 4.8%. The peak displacement of the fabricated super-high pier was 15.2 mm according to the FEM and 15.9 mm according to the test, for an error of 4.6%. The peak displacement at 2 m from the pier body was 6.8 mm according to the FEM and 7.2 mm according to the test, for an error of 5.6%. The calculated values were basically consistent with the measured values, and the error rate met the analysis requirements.

Figure 9 shows the M-φ curves of the cast-in-place super-high pier and fabricated super-high pier under RSN40 excitation. The peak of the acceleration was 1.5 g.

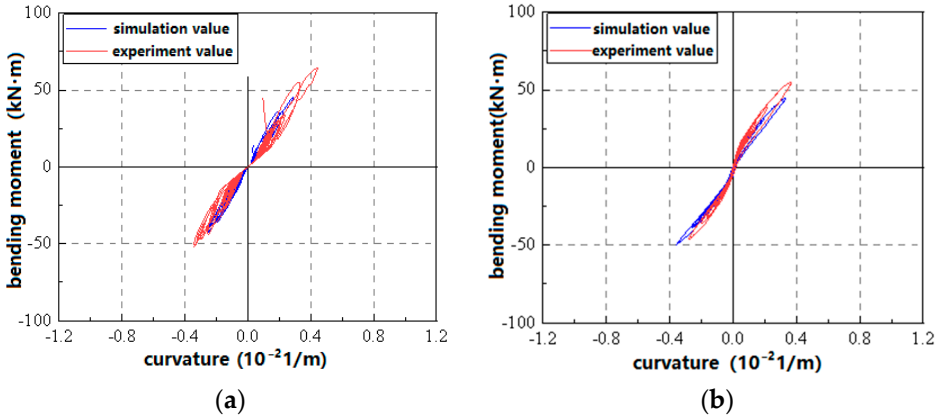

Figure 9. M-φ curves of the bottom sections of the cast-in-place super-high pier and fabricated super-high pier. (**a**) Cast-in-place pier, (**b**) Fabricated pier.

As shown in Figure 9, the M-φ curve calculated by the FEM was basically consistent with the M-φ curve of the bottom section obtained by the test. The FEM was more accurate at simulating the bending performance of the component.

In summary, for the cast-in-place super-high pier and the fabricated super-high pier, the errors between values calculated by FEM and obtained by experiment ranged from

0.67% to 2.55%. The errors in the peak pier top displacement and pier body were 5.1% and 4.8%, respectively. The displacement response time–history curves of the pier top and pier body were basically consistent. The M-φ curve calculated by FEM was basically consistent with the M-φ curve of the pier bottom obtained by the experiment, which indicated that the FEM was accurate at simulating the bending performance of the member. The accuracy of the FEM was verified in terms of the fundamental frequency, vibration pattern and structural dynamic response.

As shown in Figure 10, the FEM is established by Midas to verify the FEM established by OpenSees. The first 3 modes and frequencies calculated by Midas FEM are shown in Figure 7 and Table 4. As shown in Table 4, the error between the frequency values calculated by OpenSees and by Midas ranges from 0.08% to 1.37%, which is basically consistent. The vibration modes calculated by Midas are agreement with OpenSees.

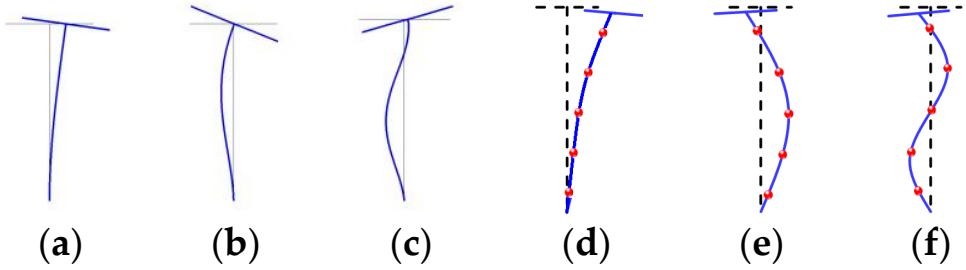

Figure 10. Vibration mode in longitudinal direction of the cast-in-place bridge specimen: (**a**) First Mode (Midas); (**b**) Second Mode (Midas); (**c**) Third Mode (Midas); (**d**) First Mode (OpenSees); (**e**) Second Mode (OpenSees); (**f**) Third Mode (OpenSees).

Table 4. Comparison of the calculation results for the dynamic characteristics.

Structural Style	Vibration Mode	Midas (Hz)	OpenSees (Hz)	Error (%)
Cast-in-place super-high pier	1	2.79	2.82	1.08
	2	18.26	18.35	0.49
	3	48.01	48.05	0.08
Fabricated super-high pier	1	2.91	2.95	1.37
	2	18.95	19.01	0.32
	3	51.59	52.02	0.83

The same modelling method can be used to establish a refined FEM for the whole bridge of the super-high-pier continuous rigid bridge.

3.2. Finite Element Model for Continuous Rigid Bridge with Super-High Piers

In this part, the FEM of continuous rigid bridge with super-high piers was established by OpenSees. The method of Section 3.1.3 was adopted for the modeling of bridge piers. In practical engineering, the main beam is mostly in an elastic state. Therefore, the main beam was simulated by an Elastic Beam Column element with the elastic modulus of 3.55×10^4 MPa. Poisson's ratio was 0.2. The modelling used a straight-for-curve approach to simulate variable cross sections. The FEM of the whole bridge is shown in Figure 11. All degrees of freedom of the pier bottom are fixed. The effect of foundation properties and geotechnical parameters is ignored.

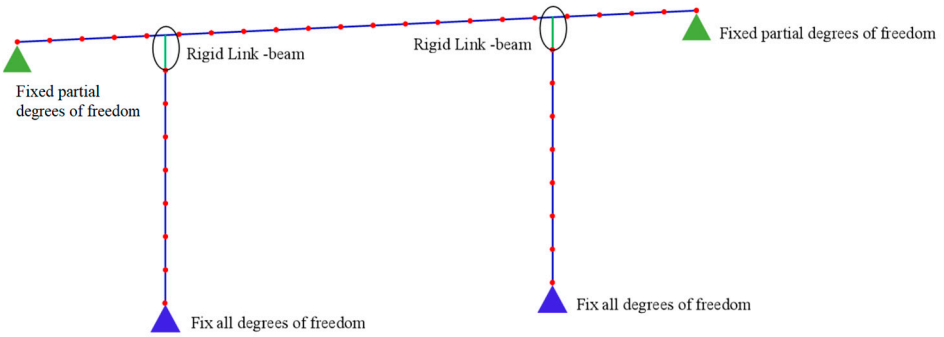

Figure 11. FEM of the bridge.

4. Earthquake Records and Analysis Cases

4.1. Earthquake Records

Based on the seismic category (Class A) and site type (Class II) of the prototype bridge, three common non-long-period ground motions (NLP), three non-pulse long-period ground motions (NPLP), and nine near-fault pulse-type ground motions (NFPT) were selected as the input ground motions. The near-fault ground motions considered three cases, $T_P < T_1$, $T_P \approx T_1$ and $T_P > T_1$. The detailed parameters of the seismic waves are shown in Table 5. The acceleration time history and Fourier spectrum are shown in Figure 12. According to the "Seismic Design Code for Highway Bridges" (JTG/T 2231-01-2020) [4] and the "Seismic Design Code for Buildings" (GB 50011-2016) [28], the peak value of the input ground motion is 0.5 g under E2 earthquake motion when the seismic fortification intensity of the bridge is 8 degrees.

Table 5. Detailed parameters of the seismic waves.

Type of the Ground Motion		Seismic Waves	Earthquake Name	Station Name	Rrup (km)	V_s30 (m/s)	T_p-Pulse Period (s)	PGA(g)
NLP		RSN503	"Taiwan SMART1(40)"	"SMART1 C00"	59.92	309.41	-	0.037
		RSN40	"Borrego Mtn"	"San Onofre—So Cal Edison"	129.11	442.88	-	0.041
		RSN55	"San Fernando"	"Buena Vista—Taft"	112.52	385.69	-	0.012
NPLP		RSN69	"San Fernando"	"LB—Terminal Island"	58.99	217.92	-	0.029
		RSN74	"San Fernando"	"Maricopa Array #1"	193.91	303.79	-	0.005
		RSN90	"San Fernando"	"UCSB—Fluid Mech Lab"	124.41	322.42	-	0.017
NFPT	$T_p < T_1$	RSN764	"Loma Prieta"	"Gilroy—Historic Bldg"	10.97	308.55	1.638	0.285
		RSN1050	"Northridge-01"	"Pacoima Dam (downstr)"	7.01	2016.13	0.588	0.618
		RSN3746	"Cape Mendocino"	"Centerville Beach_ Naval Fac"	18.31	459.04	1.967	0.318
	$T_p \approx T_1$	RSN171	"Imperial Valley-06"	"El Centro—Meloland Geot. Array"	0.07	264.57	3.423	0.317
		RSN292	"Irpinia_ Italy-01"	"Sturno (STN)"	10.84	382	3.27264	0.227
		RSN983	"Northridge-01"	"Jensen Filter Plant Generator Building"	5.43	525.79	3.535	0.571
	$T_p > T_1$	RSN184	"Imperial Valley-06"	"El Centro Differential Array"	5.09	202.26	6.265	0.244
		RSN1515	"Chi-Chi_ Taiwan"	"TCU082"	5.16	472.81	8.099	0.225
		RSN8606	"El Mayor-Cucapah_ Mexico"	"Westside Elementary School"	11.44	242	7.084	0.281

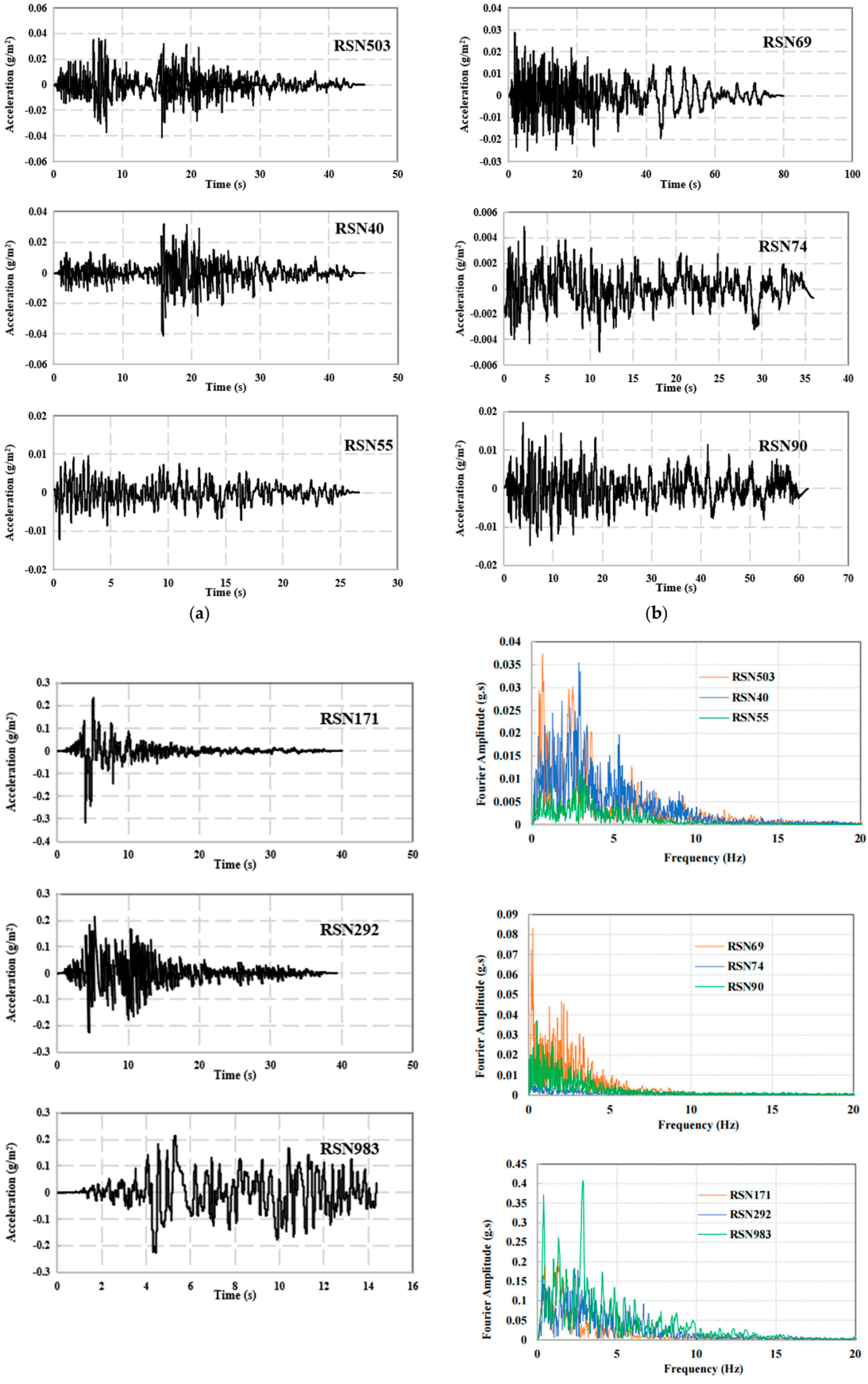

Figure 12. Earthquake waves for test: (**a**) NLP; (**b**) NPLP; (**c**) NFPT($T_p \approx T_1$); (**d**) Fourier spectrum.

4.2. Analysis Cases

A total of 15 seismic waves of three types (NLP, NPLP and NFPT) in Class II sites were selected as the input ground motions for parametric analysis of the seismic response and seismic performance of a continuous rigid-framed bridge with super-high piers. The ground motion characteristics, span of the main beam, height of the pier and number of tie beams were selected as the research parameters. Three cases of pier heights (100 m, 130 m and 160 m), three cases of main bridge spans (70 m, 120 m and 166 m) and four cases of tie beams (0, 1, 3 and 5) were selected for the research. Ground motions were excited along the longitudinal and transverse directions.

5. Results and Analysis

5.1. Influence of the Ground Motion Properties

The peak pier top displacement and peak pier bottom bending moment of the continuous rigid-framed bridge with super-high piers under different analysis cases are shown in Tables 6–9. This value is the mean value of the peak seismic response under the three ground motions in each group.

Table 6. Peak pier top displacement (cast-in-place).

Analysis Cases	Span of Main Bridge (m)	Pier Height (m)	Peak Pier Top Displacement (mm)									
			Longitudinal Direction of Bridge					Transverse Direction of Bridge				
			NLP	NPLP	NFPT			NLP	NPLP	NFPT		
					$T_P \approx T_1$	$T_P > T_1$	$T_P < T_1$			$T_P \approx T_1$	$T_P > T_1$	$T_P < T_1$
1	70	100	736	1109	1491	836	813	658	1021	1259	834	894
2		130	883	1324	1753	938	949	816	1136	1628	926	987
3		160	1108	1619	2015	1205	1198	1096	1265	1849	1196	1056
4	120	100	839	1279	1677	915	935	850	1098	1482	986	946
5		130	1095	1620	2152	1189	1177	968	1468	1968	1152	1025
6		160	1215	1997	2410	1325	1395	1135	1901	2135	1385	1245
7	166	100	937	1380	1858	1128	1112	965	1268	1593	1023	966
8		130	1205	1756	2378	1359	1295	1085	1596	2364	1223	1000
9		160	1520	2231	2925	1632	1689	1362	2008	2796	1426	1129

Table 7. Peak pier top displacement (fabricated).

Analysis Cases	Span of Main Bridge (m)	Pier Height (m)	Peak Pier Top Displacement (mm)									
			Longitudinal Direction of Bridge					Transverse Direction of Bridge				
			NLP	NPLP	NFPT			NLP	NPLP	NFPT		
					$T_P \approx T_1$	$T_P > T_1$	$T_P < T_1$			$T_P \approx T_1$	$T_P > T_1$	$T_P < T_1$
1	70	100	795	1218	1605	895	903	627	1056	1196	866	821
2		130	958	1472	1893	1032	1052	885	1285	1723	964	963
3		160	1205	1801	2136	1319	1289	968	1536	1926	1265	1123
4	120	100	942	1398	1883	1095	1105	986	1195	1534	1008	1027
5		130	1186	1793	2209	1295	1287	1024	1525	1897	1124	1194
6		160	1302	2179	2596	1521	1558	1169	1869	2238	1438	1324
7	166	100	1031	1470	2069	1251	1268	1035	1294	1642	1164	1124
8		130	1359	1920	2650	1552	1502	1164	1659	2389	1326	1265
9		160	1679	2399	3198	1793	1805	1398	2101	2934	1521	1498

Table 8. Peak pier bottom bending moment (cast-in-place).

Analysis Cases	Span of Main Bridge (m)	Pier Height (m)	Peak Pier Bottom Bending Moment (10^5 kN·m)									
			Longitudinal Direction of Bridge					Transverse Direction of Bridge				
			NLP	NPLP	NFPT			NLP	NPLP	NFPT		
					$T_P \approx T_1$	$T_P > T_1$	$T_P < T_1$			$T_P \approx T_1$	$T_P > T_1$	$T_P < T_1$
1	70	100	5.9	7.9	10.1	7.6	6.7	5.8	7.6	9.9	7.4	6.3
2		130	5.8	7.6	9.5	7.3	6.4	5.6	7.4	9.2	7.1	6.1
3		160	5.6	7.2	9.0	7.1	6.2	5.5	7.1	8.4	6.8	5.9
4	120	100	6.8	9.4	11.9	8.5	7.5	6.2	9.1	11.4	8.5	7.2
5		130	6.5	9.0	11.1	8.2	7.2	6.1	8.8	10.7	7.9	7.0
6		160	6.3	8.4	10.4	7.8	7.0	6.0	8.3	10.2	7.3	6.6
7	166	100	7.9	11.0	13.6	9.0	8.4	7.2	10.1	13.1	8.8	8.2
8		130	7.5	10.4	12.7	8.6	8.1	7.1	9.9	12.3	8.3	8.1
9		160	7.2	9.7	11.7	8.2	7.7	7.0	9.2	11.8	8.0	7.6

Table 9. Peak pier bottom bending moment (fabricated).

Analysis Cases	Span of Main Bridge (m)	Pier Height (m)	Peak Pier Bottom Bending Moment (10^5 kN·m)									
			Longitudinal Direction of Bridge					Transverse Direction of Bridge				
			NLP	NPLP	NFPT			NLP	NPLP	NFPT		
					$T_P \approx T_1$	$T_P > T_1$	$T_P < T_1$			$T_P \approx T_1$	$T_P > T_1$	$T_P < T_1$
1	70	100	4.8	7.4	8.3	5.8	5.6	4.5	7.3	8.1	5.6	5.5
2		130	4.7	7.1	7.7	5.6	5.4	4.4	7.1	7.6	5.3	5.1
3		160	4.6	6.7	7.3	5.4	5.3	4.2	6.9	7.0	5.0	5.0
4	120	100	5.7	8.7	9.8	7.1	6.7	5.2	8.7	9.5	6.5	6.5
5		130	5.5	8.3	9.2	6.9	6.5	5.1	8.3	8.9	6.1	6.2
6		160	5.3	7.8	8.6	6.6	6.3	4.9	7.6	8.4	6.0	6.0
7	166	100	6.7	10.2	11.8	8.4	7.8	6.4	10.5	12.0	8.2	7.6
8		130	6.5	9.5	10.9	8.0	7.6	6.2	9.2	10.5	8.0	7.2
9		160	6.2	8.9	10.1	7.6	7.3	5.9	8.4	9.7	7.3	7.0

As shown in Table 6, along the longitudinal direction, the peak pier top displacement of the cast-in-place super-high piers under NLPL excitations was 50~60% larger than under NLP excitations. Under NFPT ($T_P \approx T_1$) excitations, the peak displacement increased about 80~100%. Under NFPT ($T_P > T_1$ or $T_P < T_1$) excitations, the peak displacement increased about 10~20%. Along the transverse direction, the peak pier top displacement of the cast-in-place super-high piers under NLPL excitation was 20~70% larger than under NLP excitations. Under NFPT ($T_P \approx T_1$) excitations, the increase was about 70~120%. Under NFPT ($T_P > T_1$ or $T_P < T_1$) excitations, the increase was about 10~30%.

As shown in Table 7, along the longitudinal direction, the peak pier top displacement of the fabricated super-high piers under NLPL excitation was 40~70% larger than under NLP excitations. Under NFPT ($T_P \approx T_1$) excitations, the increase was about 80~100%. Under NFPT ($T_P > T_1$ or $T_P < T_1$) excitations, the increase was about 10~20%. Along the transverse direction, the peak pier top displacement of the fabricated super-high piers under NLPL excitations was 20~70% larger than under NLP excitations. Under NFPT ($T_P \approx T_1$) excitations, the increase was about 60~110%. Under NFPT ($T_P > T_1$ or $T_P < T_1$) excitations, the increase was about 10~40%.

As shown in Table 8, along the longitudinal direction, the peak pier bottom bending moment of the cast-in-place super-high piers under NLPL excitations was 30~40% larger than under NLP excitations. Under NFPT ($T_P \approx T_1$) excitations, the increase was 60~80%. Under NFPT ($T_P > T_1$ or $T_P < T_1$) excitations, the increase was 10~30%. Along the transverse direction, the peak pier bottom bending moment of the cast-in-place super-high piers under NLPL excitations was 30~50% larger than under NLP excitations. Under NFPT ($T_P \approx T_1$) excitations, the increase was about 50~80%. Under NFPT ($T_P > T_1$ or $T_P < T_1$) excitations, the increase was about 10~40%.

As shown in Table 9, along the longitudinal direction, the peak pier bottom bending moment of the fabricated super-high piers under NLPL excitations was 40~57% larger than under NLP excitations. Under NFPT($T_P \approx T_1$) excitations, the increase was about 60~80%. Under NFPT ($T_P > T_1$ or $T_P < T_1$) excitations, the increase was about 10~30%. Along the transverse direction, the peak pier bottom bending moment of the fabricated super-high piers under NLPL excitations was 40~70% larger than under NLP excitations. Under NFPT($T_P \approx T_1$) excitations, the increase was about 60~90%. Under NFPT ($T_P > T_1$ or $T_P < T_1$) excitations, the increase was about 20~30%.

According to Tables 6–9, under the same analysis cases, the peak pier top displacement and the peak pier bottom bending moment were greater under the excitation of NLPL and NFPT than under the excitation of NLP. This was because the super-high-pier bridge structure had a long period and was relatively sensitive to long-period ground motion. When $T_P < T_1$ and $T_P > T_1$, the near-fault impulsive ground motion period T_P was away from T_1. Its displacement constraints on the structure were stronger than the displacement amplification effect of the velocity pulse on the structure. Therefore, under the same conditions, the peak pier top displacement and the peak pier bottom bending moment generated by the NFPT ($T_P > T_1$, $T_P < T_1$) were smaller than those generated by NLPL. When $T_P \approx T_1$, the structure would have a similar resonance phenomenon under the excitation of NFPT. The peak pier top displacement and the peak pier bottom bending moment would increase.

The case of a "main beam span of 166 m, pier height of 100 m" is taken as an example to illustrate the change rule of displacement at different locations. As shown in Figure 13, the displacement time course curves at different heights of the CRFB-HP under three types of ground motions are given.

As shown in Figure 13, the displacement of the pier increased as the height increase at the same moment. The displacements of the super-high pier with heights H = 20 m, 30 m, 80 m and 100 m are in different directions (positive and negative) from the baseline (displacement is 0, equilibrium position) at the same moment. This indicates that the contribution of higher-order modes to the displacement response of the super-high pier is significant. In order to further explore the influence of higher-order modes, the characteristic time segments in which higher-order modes participate are counted in Table 10. The characteristic time segment was defined as the time duration that the displacements at typical pier heights were not on the same side of the center line of the pier.

As can be seen from Table 10, compared with NLP excitations, the characteristic time segment of high-order mode participation of the cast-in-place super-high pier under NLPL excitation increased by 65%, and that of the fabricated super-high pier increased by 75%. Compared with NLP, under NFPT ($T_P \approx T_1$) excitation, the characteristic time segment of high-order mode participation of the cast-in super-high pier increased by 95%, and that of the fabricated super-high pier increased by 130%. Compared with the cast-in-place super-high pier, the characteristic time segment of high-order mode participation of the fabricated super-high pier increased about 20~30%. Under NFPT ($T_P \approx T_1$) excitations, the contribution of higher order modes was most obvious. The NFPT usually contains reverse and asymmetric velocity pulses. The pier-bottom region responds first when NFPT positive pulses are fed from the bottom. There is an obvious phase difference between the pier bottom and pier top regions because of the high pier height and hysteretic response of the top of the pier. The contribution of higher order modes is more significant for fabricated super-high piers compared to cast-in-place super-high piers.

The distribution of peak curvature along the pier height under different ground motions is given in Figure 14. This value is the mean value of the peak curvature under the three ground motions in each group.

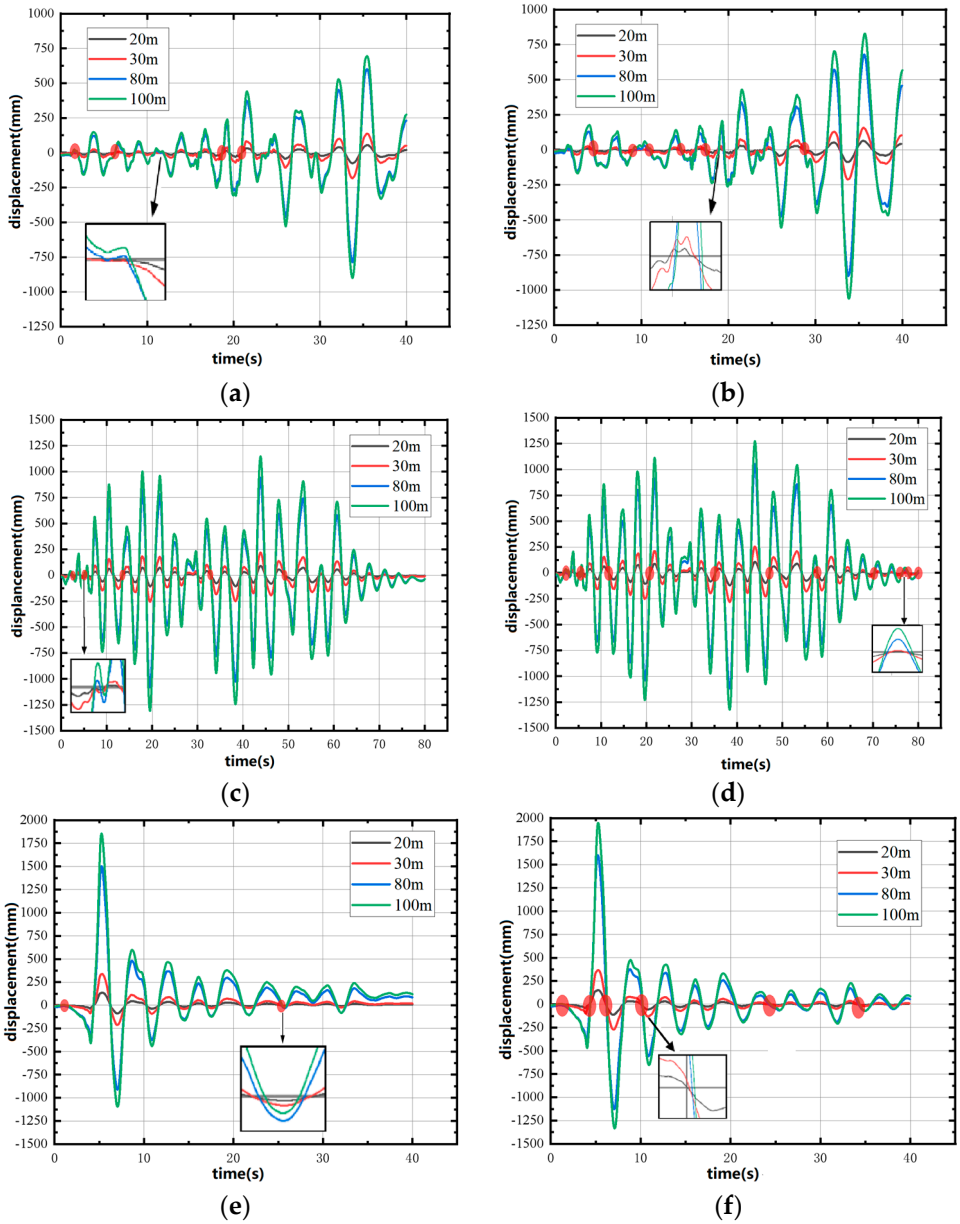

Figure 13. Time–history curve of the pier displacement: (**a**) Cast-in-place super-high pier, under NLP; (**b**) Fabricated super-high pier, under NLP; (**c**) Cast-in-place super-high pier, under NPLP; (**d**) Fabricated super-high pier, under NPLP; (**e**) Cast-in-place super-high pier, under NFPT ($T_P \approx T_1$); (**f**) Fabricated super-high pier, under NFPT ($T_P \approx T_1$).

Table 10. Statistics of characteristic time segments.

Type of the Ground Motion	Cumulative Duration/s	
	Cast-in-Place Pier	Fabricated Pier
NLP	2.0	2.4
NPLP	3.3	4.2
NFPT	3.9	5.1

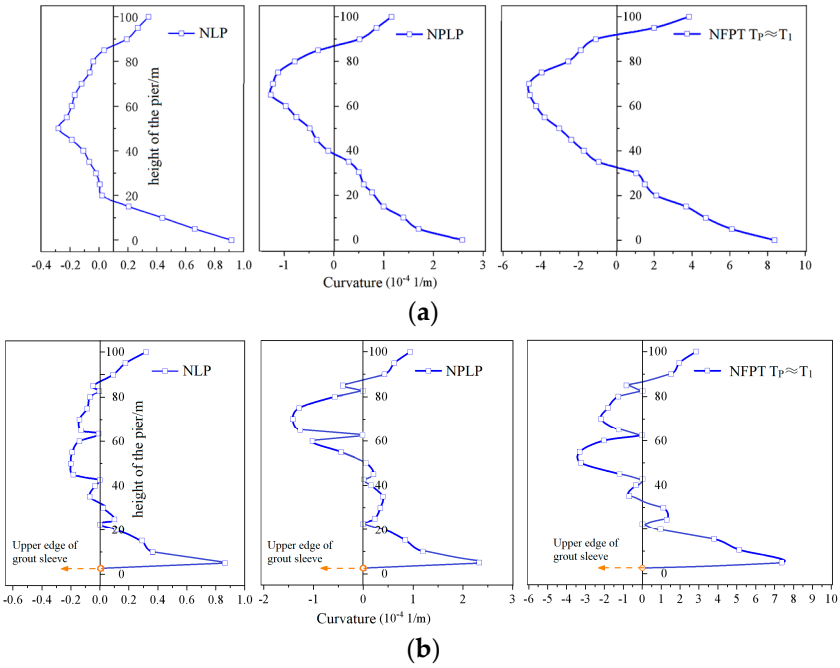

Figure 14. Curvature distribution along the pier height: (**a**) Cast-in-place super-high pier; (**b**) Fabricated super-high pier.

As shown in Figure 14, the peak curvatures at the top of the pier, the middle of the pier and the bottom of the pier under NLP excitation were 3.39×10^{-5} 1/m, 2.85×10^{-5} 1/m and 9.12×10^{-5} 1/m, respectively. Under the NPLP excitation, they were 1.16×10^{-4} 1/m, 1.27×10^{-4} 1/m and 2.58×10^{-4} 1/m, respectively. In summary, it appeared that the maximum curvature continued to be located at the pier bottom. The range and development degree of the plastic hinge have a great relationship with the spectral characteristics of ground motion. The curvature demands generated by NFPT ($T_P \approx T_1$) and NPLP were notably higher. The long-period structures are sensitive to long-period ground motion, while NFPT ($T_P \approx T_1$) and NPLP are more likely to provoke the participation of higher-order modes. Consequently, under the excitation of NFPT ($T_P \approx T_1$) and NPLP, the plastic hinge within the midsection of the pier is more pronounced than that under the NLP.

As earthquake ground motions were excited in longitudinal direction, the *M-φ* curves of the pier are shown in Figures 15–17.

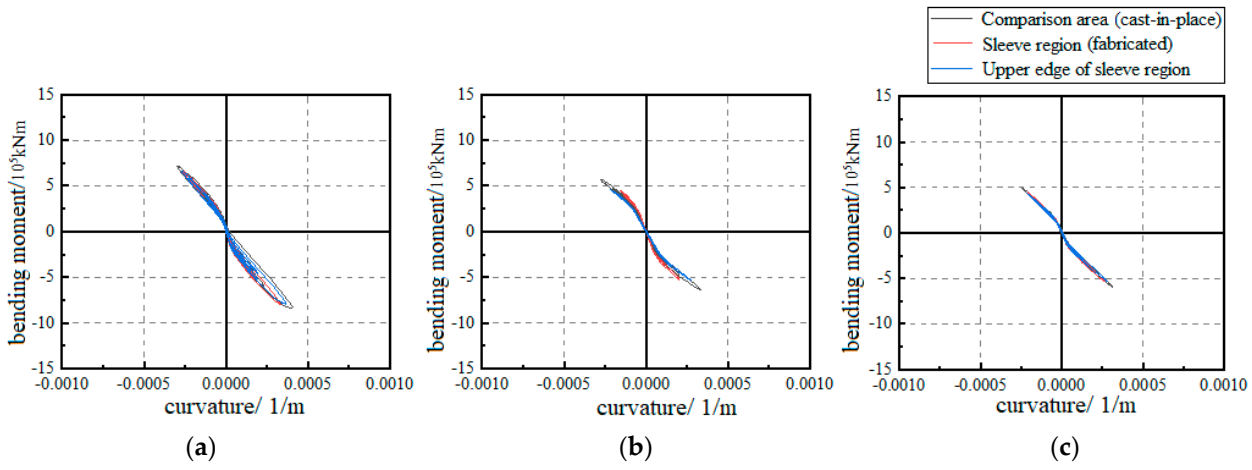

Figure 15. *M-φ* curve of bridge pier (NLP): (**a**) Pier bottom; (**b**) Pier body; (**c**) Pier top.

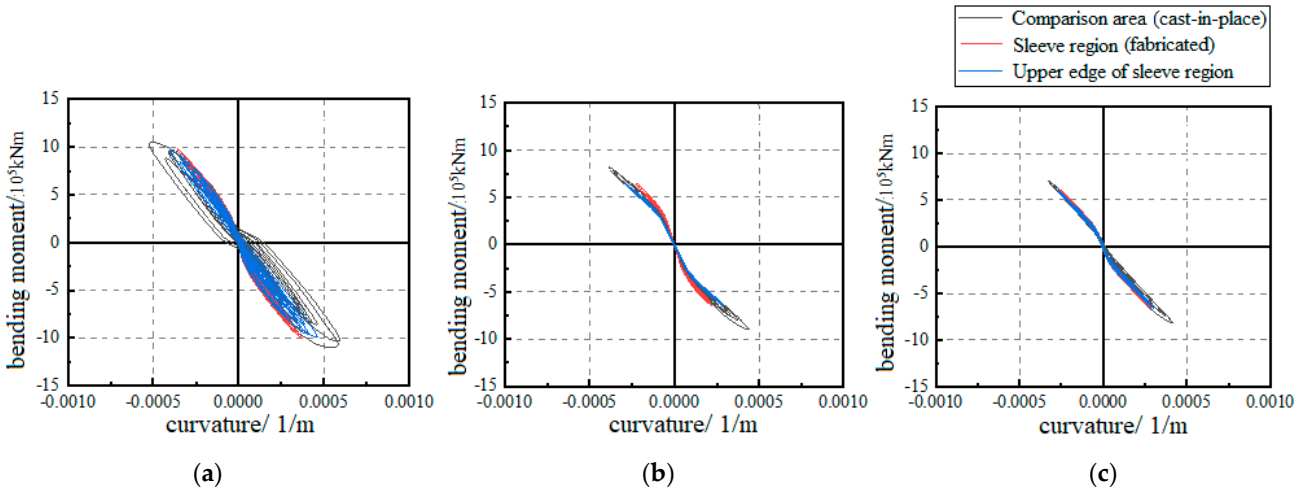

Figure 16. *M-φ* curve of bridge pier (NPLP): (**a**) Pier bottom; (**b**) Pier body; (**c**) Pier top.

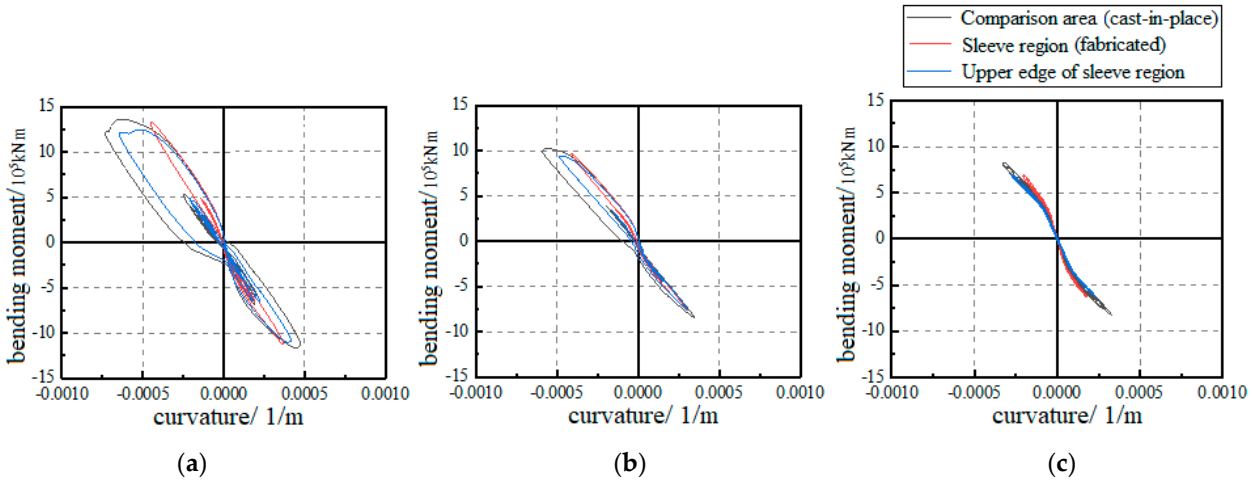

Figure 17. *M-φ* curve of bridge pier ($T_P \approx T_1$): (**a**) Pier bottom; (**b**) Pier body; (**c**) Pier top.

As shown in Figures 15–17, under the excitation along the longitudinal direction, the bending moment and curvature of piers at different positions present the same rule: pier bottom > pier body > pier top. At the same position, the bending moment and curvature of the cast-in-place super-high pier (corresponding area of sleeve) were greater than those of the fabricated super-high pier. Under the excitation of NLP, plastic hinges appear at the bottom of the pier and in the middle of the pier body. Taking the *M-ϕ* curve of the pier bottom as an example, the stiffness of the sleeve area of the fabricated super-high pier increased, resulting in plastic hinges appearing at the upper edge of the sleeve. Compared to the cast-in-place pier, the displacement of the plastic hinge had shifted upwards. The plastic hinge in the middle of the pier body and the top of the pier was not obvious. Under the excitation of NLPL and NFPT ($T_P \approx T_1$), the plastic hinge could be observed in the middle and top of the pier. The energy dissipation capacity of the middle and top of the pier cannot be ignored.

As earthquake ground motions were excited in the transverse direction, the *M-φ* curves of the pier are shown in Figures 18–20.

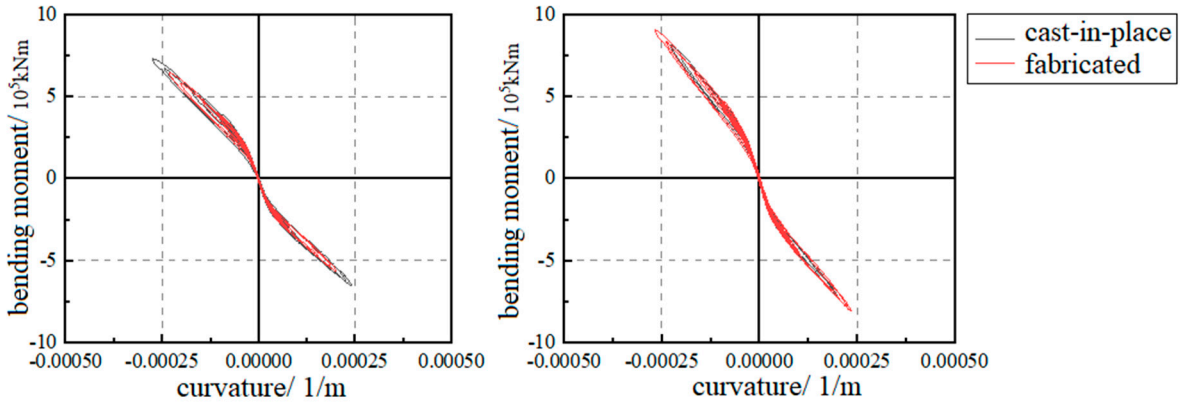

Figure 18. *M*-*φ* curve of bridge pier (NLP): (**a**) Pier bottom; (**b**) Tie beam.

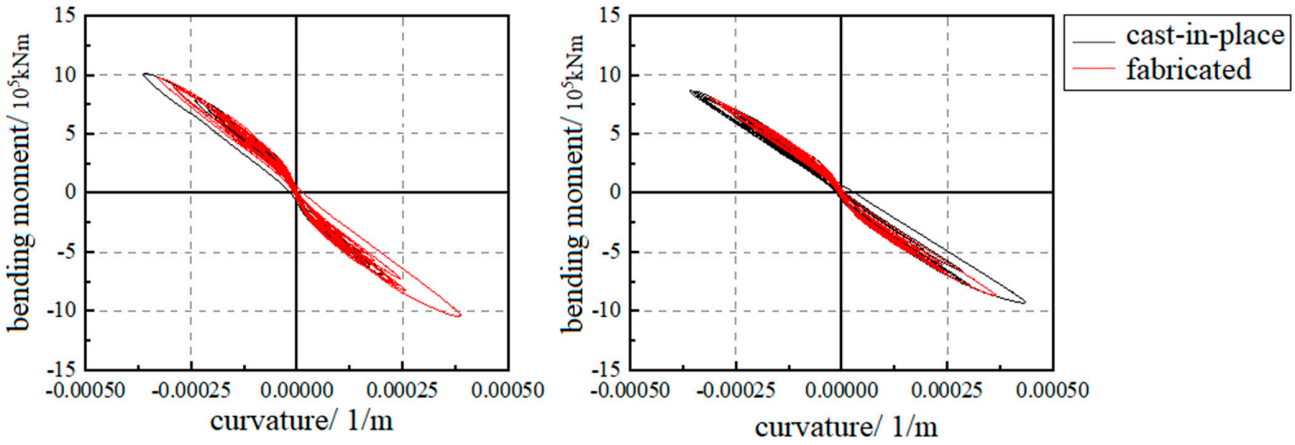

Figure 19. *M*-*φ* curve of bridge pier (NLPL): (**a**) Pier bottom; (**b**) Tie beam.

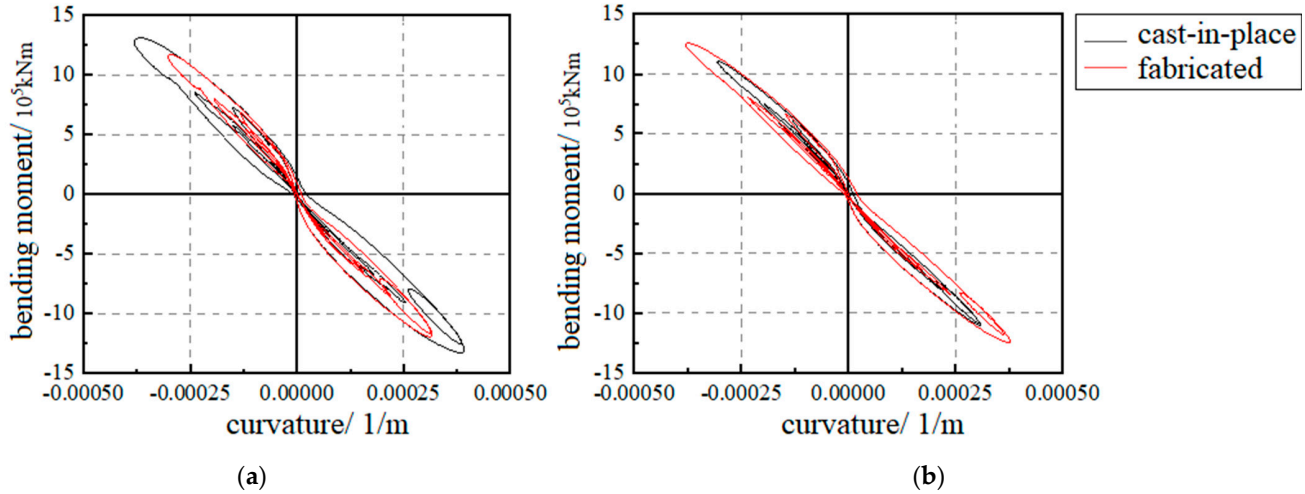

Figure 20. *M*-*φ* curve of the pier ($T_P \approx T_1$): (**a**) Pier bottom; (**b**) Tie beam.

As shown in Figures 18–20, the plastic hinge appeared at the bottom of the cast-in-place and fabricated super-high piers under NLP excitations. The *M*-*ϕ* curve of the cast-in-place super-high pier was fuller. The energy consumption was greater. A plastic hinge was also produced at the tie beam. The tie beam of the fabricated bridge had higher

energy consumption. Under the excitation of NLPL, a plastic hinge appeared at the bottom of the super-high pier. The *M*-ϕ curve of the fabricated bridge was fuller. The energy consumption was greater. A plastic hinge was also produced at the tie beam. The tie beam of the cast-in-place bridge had higher energy consumption. Under NFPT ($T_P \approx T_1$) excitations, a plastic hinge area appeared at the bottom of the super-high pier. The *M*-ϕ curve of cast-in-situ bridge pier bottom was fuller. A plastic hinge was also produced at the tie beam. The tie beam of the fabricated bridge had higher energy consumption. The tie beam can effectively share the energy input to the bridge, delay the damage of the main pier to a certain extent and improve the seismic performance of the bridge.

In summary, under the excitation of ground motions, the damage mode of the super-high pier is obviously different from that of the medium and low piers. Plastic hinges are usually formed at the bottom of the medium and low piers, while plastic hinges are usually formed both at the bottom and in the middle of the super-high piers. The peak of pier top displacement and pier bottom curvature do not appear at the same moment with the participation of the high order mode.

5.2. Influence of the Main Bridge Span and Pier Height

As shown in Tables 6 and 7, under the excitation of three types of earthquakes, when the span was the same, the peak displacement at the top of the super-high piers increased with the pier height, both in the longitudinal and transverse directions. Taking L = 166 m under the longitudinal excitation of NLP as an example, when the heights of the piers were 100 m, 130 m and 160 m, the peak pier top displacements were 937 mm, 1205 mm and 1520 mm, respectively, and the corresponding change rates were 28.6% and 26.1%, respectively. When the pier height was the same, the peak displacement at the pier top increased with the span of the main beam. Taking H = 100 m under NLP as an example, when the spans were 70 m, 120 m and 166 m, the peak pier top displacements were 736 mm, 839 mm and 937 mm, respectively, and the corresponding change rates were 14.0% and 11.7%, respectively. It can be seen that the change of pier height has more influence on the displacement of the pier top than the change of the span. As can be seen from Tables 6 and 7, the peak displacement of the fabricated super-high pier is greater than that of the cast-in-place super-high pier under the same case. The main reason is that there are many segmentary joints in the fabricated super-high pier. Under the excitation of ground motion, the joint is repeatedly opened and closed, which damages the local concrete. The decline of pier stiffness is accelerated.

As shown in Tables 8 and 9, under the excitation of three types of earthquakes, when the pier height was the same, the peak bending moment at the bottom of the super-high piers increased with the span both in the longitudinal and transverse directions. The peak pier bottom bending moment induced by NPLP and NFPT ($T_P \approx T_1$) was larger. When the span was the same, the peak bending moment at the bottom of the super-high pier decreased with the pier height both in the longitudinal and transverse directions. The bending moment of the pier bottom of damage fabricated super-high pier is smaller than that of the cast-in-place super-high pier.

5.3. Influence of Number of Tie Beams

To reveal the influence of the number of tie beams on the seismic response of continuous rigid-framed bridge with super-high piers, the transverse seismic response of a super-high-pier continuous rigid-framed bridge with the span L = 166 m and pier height H = 100 m was analyzed. Four cases of tie beams (0, 1, 3, and 5) were considered for the research. Under the excitation of three different types of ground motion, the peak displacement of the pier top was shown in Figure 21.

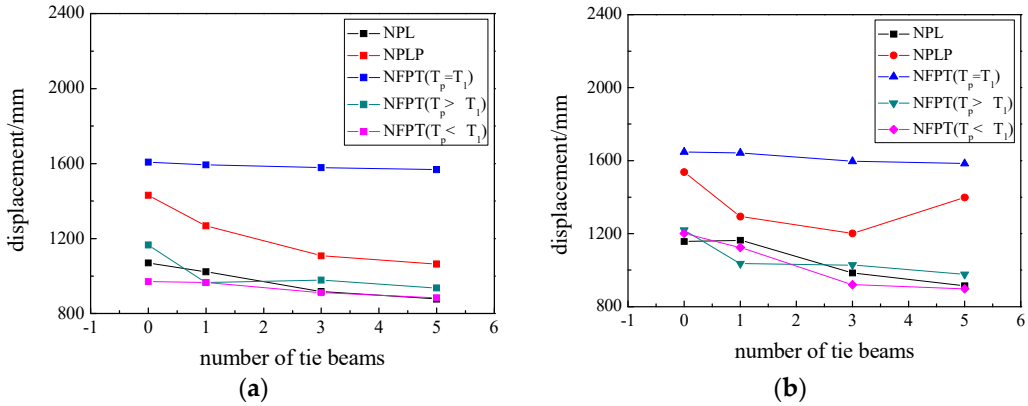

Figure 21. Comparison of the displacement: (**a**) Cast-in-place pier; (**b**) Fabricated pier.

Figure 21 shows that under the same ground motion, the peak displacement at the top of the continuous rigid-framed piers with super-high piers slowly decreased as the number of tie beams increased. Taking the bridge under the excitation of the NFPT ($T_P \approx T_1$) as an example, the peak displacements of the pier top were 1608 mm, 1593 mm, 1578 mm and 1568 mm when the bridge had 0, 1, 3 and 5 tie beams, respectively. Under different ground motions, the peak pier top displacement exhibited the following trend: $\Delta_{NLP} < \Delta_{NFPT}$ ($T < T_1$, $T_P > T_1$) < $\Delta_{NPLP} < \Delta_{NFPT}$ ($T_P \approx T_1$). Taking the continuous rigid-framed bridge with three tie beams as an example, the peak pier top displacement under the excitation of NLP, NFPT ($T_P < T_1$, $T_P > T_1$), NPLP and NFPT ($T_P \approx T_1$) were 918 mm, 979 mm, 1108 mm and 1578 mm, respectively.

Under the excitation of three different types of ground motion, the peak bending moment of the pier bottom is shown in Figure 22.

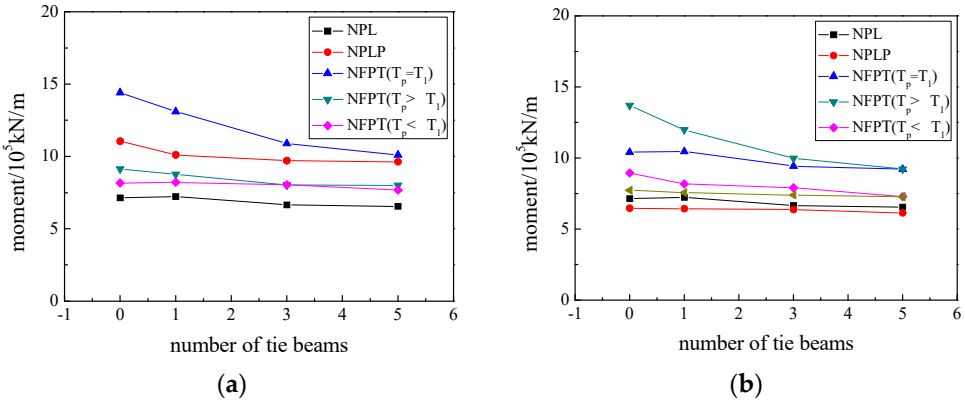

Figure 22. Comparison of the bending moment: (**a**) Cast-in-place pier; (**b**) Fabricated pier.

As shown in Figure 22, under the same ground motion, with an increase in the number of tie beams, the peak pier bottom bending moment slowly decreased. Taking the bridge under the excitation of the NFPT ($T_P \approx T_1$) as an example, the peak pier bottom bending moments were 14.41 × 105 kN·m, 13.10 × 105 kN·m, 10.90 × 105 kN·m and 10.10 × 105 kN·m when the bridge had 0, 1, 3 and 5 tie beams, respectively. Under different ground motions, the peak pier bottom bending moment exhibited the order of $M_{NLP} < M_{NFPT}$ ($T_P < T_1$, $T_P > T_1$) < $M_{NPLP} < M_{NFPT}$ ($T_P \approx T_1$). Taking the continuous rigid-framed bridge with one tie beam as an example, the bending moments of the pier top under NLP, NFPT ($T_P < T_1$, $T_P > T_1$), NPLP and NFPT ($T_P \approx T_1$) were 7.23 × 105 kN·m, 8.48 × 105 kN·m, 10.11 × 105 kN·m and 13.10 × 105 kN·m, respectively.

The *M*-φ curve of the pier bottom is shown in Figure 23, under NFPT ($T_P \approx T_1$) excitation.

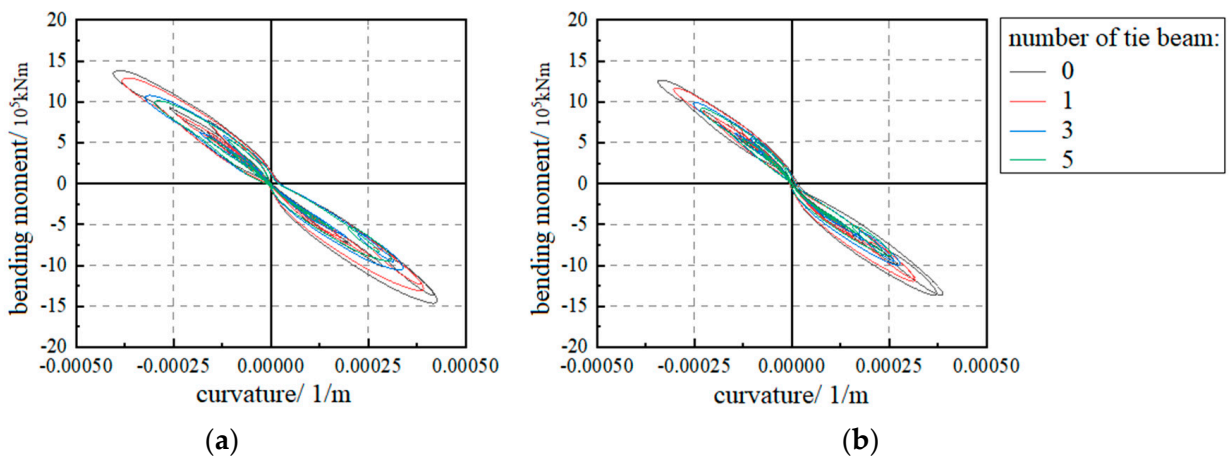

Figure 23. *M*-φ curve of bridge pier bottom: (**a**) Cast-in-place pier; (**b**) Fabricated pier.

As can be seen from Figure 23, under the excitation of NFPT ($T_P \approx T_1$), plastic hinges appeared at the bottom of the piers of both cast-in-place and fabricated super-high-pier continuous rigid-framed bridges and showed the same pattern: the energy dissipation at the bottom of the piers of the bridges gradually can be decreased with the increase in the number of tie-beam channels. The arrangement of tie beams is conducive to reducing the damage at the bottom of the super-high pier and sharing the energy input to the bridge effectively.

6. Conclusions

This study carried out elastic-plastic time history analysis of continuous rigid-framed bridges with super-high piers (CRFB-HP) based on the OpenSees platform. And the influence of parameters on the seismic performance of CRFB-HP was systematically investigated, including main bridge span, pier height and number of tie beams. The main conclusions are as follows:

(1) CRFB-HP have the characteristic of long vibration periods and are more sensitive to long-period ground motions. Along the longitudinal direction, the peak pier top displacement and pier bottom bending moments of CRFB-HP under NPLP excitations are 40~70% and 30~50% larger than under NLP excitations, respectively. Moreover, the peak pier top displacement and pier bottom bending moment of CRFB-HP under NFPT ($T_P \approx T_1$) are 80~100% and 60~80% larger than under NPLP excitations, respectively. Along the transverse direction, the peak pier top displacement and pier bottom bending moment of the CRFB-HP under NPLP excitations increase by 20~70% and 30~70% compared with those under NLP excitations. In addition, the peak pier top displacement and pier bottom bending moment of the CRFB-HP under NFPT ($T_P \approx T_1$) increase by 60~120% and 50~90% compared with those under NPLP excitations. Thus, the difference in the increase under different types of excitations along the transverse bridge direction is greater than that of along the longitudinal direction.

(2) Under the same ground motions, the change rule of the seismic response of CRFB-HP is the same along the longitudinal direction and transverse direction. With the same span, the peak pier top displacement increases with the pier height increasing, while the peak pier bottom bending moment decreases with the pier height increasing. With the same pier height, the peak pier top displacement and peak pier bottom bending moment both increase with the span length increasing. Moreover, the pier height change has a greater effect on the pier top displacement than that of the span change. Taking the NLP excitation as an example, the peak pier top displacement increases by 20~60% with the pier height change, and by 10~40% with the span change.

(3) CRFB-HP shows obvious high-order response participation (HRP) under different ground motions. Compared with NLP, the feature period of the HRP of cast-in-place

and fabricated CRFB-HP increases by 65% and 75% compared to NLPL excitations, respectively. Compared with NLP, the feature period of the HRP of cast-in-place and fabricated CRFB-HP increase by 95% and 113% compared to NFPT ($T_P \approx T_1$) excitation. Thus, the NFPT ($T_P \approx T_1$) ground motions can significantly increase the HRP. Moreover, compared with cast-in-place CRFB-HP, the HRP of fabricated super-high piers is greater (+20~+30%). The plastic hinge may occur in the bottom, middle and top of the pier body resulted in the HRP, especially for the fabricated CRFB-HP.

(4) Under the same ground motion, the peak pier top displacement and pier bottom bending moment both decrease with the increase in the number of tie beams. Compared to the cast-in-place CRFB-HP, the peak pier top displacement is larger and the peak pier bottom bending moment is smaller for the fabricated CRFB-HP. The damage of the pier bottom decreases with the increase of the number of beams. The reason is that the energy consumption of the tie beam increases with the number of beams. Therefore, a reasonable arrangement of tie beams can improve the lateral seismic performance of CRFB-HP.

(5) Due to space limitations, the sensitivity analysis of the influence parameters on the seismic performance of CRFB-HP is not conducted in this study. The sensitivity analysis of the influence parameters on the seismic performance of CRFB-HP, as well as the seismic design method of the CRFB-HP, need to be carried out in future.

Author Contributions: Conceptualization, X.-Y.Y. and Z.Z.; methodology, S.-S.C.; validation, X.-Y.Y. and C.-H.L.; data curation, C.-H.L.; writing—original draft preparation, Y.-F.Z.; writing—review and editing, Y.-F.Z.; funding acquisition, X.-Y.Y. and Z.Z. All authors have read and agreed to the published version of the manuscript.

Funding: This research was funded by the Natural Science Foundation of China under Grant no. 52178446 and the Open Research Fund of Key Laboratory of Beijing University of Technology under Grant no. 2022B02.

Data Availability Statement: All data generated or analyzed during this study are included in this article.

Conflicts of Interest: The authors declare no conflicts of interest.

References

1. Huang, J.; Tan, P.; Zhang, Y.; Zhou, F. Endurance time analysis of seismic performances of long-span continuous rigid-frame bridges with corrugated steel webs. *Structures* **2022**, *43*, 990–1001. [CrossRef]
2. Li, X.; Li, L. Research on Green Evaluation of Mountainous Highway Construction. In Proceedings of the International Symposium on Advancement of Construction Management and Real Estate, Wuhan, China, 28–30 November 2020; Springer: Singapore, 2020; pp. 727–745.
3. Zheng, Y.; Wang, J.; Xu, W.; Li, N.; Zhang, W.; Chen, Y. Impact of Near-Fault Ground Motions on Longitudinal Seismic Response of CHRF Bridges. *Sustainability* **2022**, *14*, 3591. [CrossRef]
4. *JTG/T 2231-01-2020.0*; Specifications for Seismic Design of Highway Bridges. China Merchants Chongqing Transportation Research and Design Institute Co., Ltd.: Chongqing, China, 2020.
5. Standards I. Eurocode 8-Design Provisions for Earthquake Resistance of Structures—Part 2: Bridges.
6. Xu, C.; Xiang, N.; Li, C. Influence of higher-order modes of slender tall pier bridge columns on the seismic performance of pile foundations. *Soil Dyn. Earthq. Eng.* **2021**, *142*, 106543.
7. Xu, C.; Guan, Z.; Li, J.; Spencer, B.F., Jr. Shake table tests of tall-pier bridges to evaluate seismic performance. *J. Bridge Eng.* **2018**, *23*, 4018051–4018058.
8. Tubaldi, E.; Tassotti, L.; Dall'Asta, A.; Dezi, L. Seismic response analysis of slender bridge piers. *Earthq. Eng. Struct. Dyn.* **2014**, *43*, 1503–1519. [CrossRef]
9. Li, J.Z.; Tang, H.; Guan, Z.G. Shake table test and numerical analysis of a bridge model supported on elastomeric pad bearings. *J. Earthq. Eng.* **2016**, *21*, 604–634. [CrossRef]
10. Shao, C.; Qi, Q.; Wang, W.; Wang, Y.; Dai, X.; Huang, H. Study on longitudinal seismic mitigation performance of a long-span railway continuous steel truss girder bridge with super high piers using fluid viscous dampers. *China Railw. Sci.* **2022**, *42*, 27–38.
11. Xu, T.; Li, Q.; Zhao, R.; Ding, J.; Zhan, Y. On the early-age bond-slip behavior of an eccentric bar embedded in a grouted sleeve. *Eng. Struct.* **2019**, *190*, 160–170. [CrossRef]
12. Shen, B.; Xu, W.; Wang, J.; Chen, Y.; Yan, W.; Huang, J.; Tang, Z. Seismic control of super high-rise structures with double-layer tuned particle damper. *Earthq. Eng. Struct. Dyn.* **2021**, *50*, 791–810. [CrossRef]

13. Xu, W.; Luo, Z.; Yan, W.; Chen, Y.; Wang, J. Impact of pulse parameters on the seismic response of long-period bridges. *Struct. Infrastruct. Eng.* **2020**, *16*, 1461–1480. [CrossRef]
14. Borzi, B.; Ceresa, P.; Franchin, P.; Noto, F.; Calvi, G.M.; Pinto, P.E. Seismic Vulnerability of the Italian Roadway Bridge Stock. *Earthq. Spectra* **2015**, *31*, 2137–2161. [CrossRef]
15. Nettis, A.; Iacovazzo, P.; Raffaele, D.; Uva, G.; Adam, J.M. Displacement-based seismic performance assessment of multi-span steel truss bridges. *Eng. Struct.* **2022**, *254*, 113832. [CrossRef]
16. Nettis, A.; Rafaele, D.; Uva, G. Seismic risk-informed prioritisation of multispan RC girder bridges considering knowledge-based uncertainty. *Bull. Earthq. Eng.* **2024**, *22*, 693–729. [CrossRef]
17. Chaudhary, M.T.A. Sensitivity of seismic response of pile-supported, multi-span viaduct bridges to interaction between soil-foundation and structural parameters. *Innov. Infrastruct. Solut.* **2023**, *8*, 180. [CrossRef]
18. Wang, S.; Xu, W.; Huang, X.; Yan, X.; Ma, J.; Sun, H.; Chen, Y. Research on the pounding response and pounding effect of a continuous rigid-Frame bridge with fabricated super-high piers connected by grouting sleeves. *Sustainability* **2022**, *14*, 11334. [CrossRef]
19. Tavares, V.; Gregory, J.; Kirchain, R.; Freire, F. What is the potential for prefabricated buildings to decrease costs and contribute to meeting EU environmental targets? *Build. Environ.* **2021**, *206*, 108382. [CrossRef]
20. Zhao, L.F.; Hao, H.; Bi, K.M.; Li, X. Numerical study of the seismic responses of precast segmental column bridge under spatially varying ground motions. *J. Bridge Eng.* **2018**, *23*, 401–425. [CrossRef]
21. Liu, Y.; Zhou, B.; Cai, J.; Lee, D.S.H.; Deng, X.; Feng, J. Experimental study on seismic behavior of precast concrete column with grouted sleeve connections considering ratios of longitudinal reinforcement and stirrups. *Bull. Earthq. Eng.* **2018**, *16*, 6077–6104. [CrossRef]
22. Ding, Y.; Xu, W.; Chen, Y.; Wang, J.; Yan, W. Experimental research on seismic performance of precast cogging high-strength bolt composite joint and influence of its arrangement location. *Eng. Struct.* **2020**, *225*, 111294. [CrossRef]
23. Xin, G.; Xu, W.; Wang, J.; Yan, X.; Chen, Y.; Yan, W.; Li, J. Seismic performance of fabricated concrete piers with grouted sleeve joints and bearing-capacity estimation method. *Structures* **2021**, *33*, 169–186. [CrossRef]
24. Liu, H.; Chen, J.; Xu, C.; Du, X. Seismic performance of precast column connected with grouted sleeve connectors. *J. Build. Eng.* **2020**, *31*, 101410. [CrossRef]
25. Lu, Z.; Huang, J.; Dai, S.; Liu, J.; Zhang, M. Experimental study on a precast beam-column joint with double grouted splice sleeves. *Eng. Struct.* **2019**, *199*, 109589. [CrossRef]
26. Wang, S.; Xu, W.; Wang, J.; Xin, G.; Chen, Y.; Zhao, Z.; Bai, Y. Experimental research on anti-seismic reinforcement of fabricated concrete pier connected by grouting sleeve based on CFRP and PET materials. *Eng. Struct.* **2021**, *245*, 112838. [CrossRef]
27. Sarkar, N.; Dasgupta, K. Comparative Study of Concrete Models in OpenSEES for Performing Nonlinear Analysis. In Proceedings of the International Conference on Structural Engineering and Construction Management, Kandy, Sri Lanka, 17–19 December 2021; Springer: Cham, Switzerland, 2021; pp. 1135–1143.
28. *GB 50011-2016*; Code for Seismic Design of Buildings. Ministry of Housing and Urban-Rural Development. People's Republic of China: Beijing, China, 2016.